ACS OMEGA

Open Access

http://pubs.acs.org/journal/acsodf

Article

Facile Synthesis of a Pyrovanadate $Ni_2V_2O_7$ Hollow Sphere/Reduced Graphene Oxide Nanocomposite as a Solid-State Hybrid Supercapacitor

Selvan Maruthasalamoorthy and Navamathavan Rangaswamy*

Cite This: *ACS Omega* 2024, 9, 51481−51493

Read Online

ACCESS | Metrics & More | Article Recommendations | Supporting Information

ABSTRACT: Nickel pyrovanadate (NVO) and compositing rGO in different concentrations with NVO are synthesized via the solvothermal process. XRD patterns reveal the formation of crystalline NVO and amorphous rGO in the nanocomposite. The morphology of the material resembles the formation of an NVO hollow nanosphere through a template-free synthesis route with the effect of ethylene glycol. From the CV oxidation and reduction curve, the battery-type faradic reaction is observed. The specific surface area increment via the rGO concentration increment in nanocomposites is due to the partially encapsulated hollow sphere on the 2D active surface area of rGO owing to better specific capacitance and electrochemical stability. In addition, the maximum specific capacitance of 3807 F g^{-1} at 1 A g^{-1} for NVO@rGO 20 is obtained via a three-electrode system. The solid-state device shows the specific capacitance retention of ∼70% even after 10,000 cycles for a scan rate of 10 A g^{-1}. The liquid electrolyte device shows the specific capacitance retention of ∼90% from its initial value and the successive charge−discharge process seen over the 10,000 cycles for the scan rate 10 A g^{-1}. The suitable device is identified from this work in terms of high stability, high specific capacitance, and excellent reversibility for electrochemical performance.

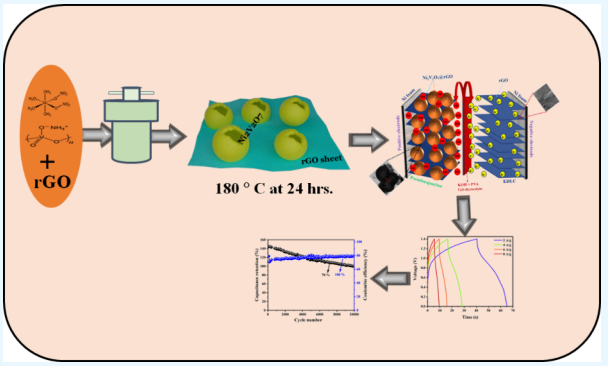

1. INTRODUCTION

Over the past century, the expansion of human activities has led to a significant increase in energy demand and resource consumption worldwide, which has profoundly affected our planet's ecosystems and biodiversity.[1] The depletion of fossil fuels and the related environmental problems over the past decades have driven the push for developing clean and renewable energy sources like solar, wind, water, and coal.[2] Supercapacitors have recently garnered significant research interest among various energy storage devices for their high power density, rapid charge and discharge rates, exceptional cycling lifespan, and lightweight design.[3] Furthermore, they are categorized into two types, namely, electric double layer capacitor (EDLC) and pseudocapacitor. Conway identified several faradaic mechanisms that contribute to their capacitive electrochemical features.[4] The faradaic mechanism undergoes an interaction between electrolyte ions and electrodes known as pseudocapacitive reaction, and the electrode surface undergoes a fast and reversible redox process. During the electrochemical process, the cyclic voltammetry (CV) and galvanostatic charge and discharge (GCD) graphs depicted are quasi rectangular and triangle, respectively. In simpler terms, a pseudocapacitive electrode material shows a battery-type redox reaction during which electrode materials undergo phase changes.[2] Surface redox capacitors or intrinsic pseudocapacitors proceed by charge transfer to the electrode surface, and these materials exhibit inherent electrochemical properties as these intrinsic pseudocapacitive materials, owing to their multiple valence states, initiate fast and reversible redox reactions at the electrode surface.[5] Redox pseudocapacitance occurs when ions are electrochemically adsorbed onto or near the surface of a material, involving a simultaneous faradaic charge transfer. Intercalation pseudocapacitance is a phenomenon in which ions insert themselves into the tunnels or layers of a redox-active material, resulting in faradaic charge transfer. This process occurs without causing any changes to the material's crystallographic phase.[6] Similarly, the EDLC occurs by the formation of an electric double layer on the porous electrode surface due to the electrolyte ion adsorption and desorption, which categorized the Helmholtz double-layer, Gouy−Chapman−Stern model. The Helmholtz double layer forms when a voltage is applied to the electrodes; ions from the electrolyte migrate to the surface of the electrodes. In addition,

Received: September 23, 2024
Revised: November 18, 2024
Accepted: November 20, 2024
Published: December 17, 2024

the Gouy−Chapman−Stern model closest to the electrode surface, where ions are specifically absorbed, is called the stern model, while the Gouy−Chapman model explains the diffusion layer formation on the electrode surface, where ions are loosely associated and distributed according to the Boltzmann distribution. Vanadium (Z = 23), a transition metal in group 5 of the periodic table, is a hard, steel-gray metal. Its valence electron configuration is $3d^3\ 4s^2$, giving it five valence electrons in the outermost shell. These five valence electrons are available for bonding.[7] Therefore, vanadium can exist in various oxidation states, specifically +5, +4, +3, and +2, which contribute to its excellent pseudocapacitance.[8] Vanadium oxides have garnered interest for over four decades among transition metal oxides (TMOs) due to their abundant natural resources, the multiple valence states of vanadium, and their diverse structures.[9] The structure $T_2X_2O_7$ (T = Cu, Co, Ni, Fe, Mn; X = P, As, V) has been widely studied for supercapacitor application.[10] This structure has gained considerable interest as an active electrode material for pseudosupercapacitors, owing to its multiple oxidation states, its layered structure, and the synergistic effect between transition metals. Additionally, transition metal vanadate's nanostructure offers a high specific surface area, ample electroactive sites, and reduced ion diffusion pathways. These advantages significantly enhance the electrochemical performance of pseudosupercapacitors.[1,8,10,11] However, pyro vanadate has been given focus due to its various oxidation states. The magnetic Ni^{2+} in $Ni_2V_2O_7$ has two crystallographic sites, Ni1 and Ni_2. Moreover, the zigzag shapes that are created by multiple corners are shared by NiO_6 octahedra by the c axis and they are separated by incorporating edge-sharing, nonmagnetic VO_4 tetrahedra.[12] This results in a quasi-one-dimensional structural arrangement and antiferromagnetic property. Ezhil Arasi et al. synthesized the low-dimensional nanorod shape of $Ni_2V_2O_7$ by the coprecipitation method, which possesses excellent electrochemical stability and a capacitance retention of 94.1% up to 3000 cycles.[13] Furthermore, the specific capacitance varies with different approaches involved in designing and preparing nanostructures with various dimensions, ranging from zero-dimensional to three-dimensional. Another method focuses on the hybridization of metal vanadates with carbonaceous materials.[14] A well-conceived design of multicomponent metal oxide hierarchical nanostructures is an effective and promising approach to enhance the electrochemical performance of electrode materials. Novel hydrangea-like $ZnCo_2O_4$/$Ni_3V_2O_8$ hierarchical nanostructures were constructed by adjusting the ratio of $ZnCo_2O_4$ to $Ni_3V_2O_8$. As a result, the $ZnCo_2O_4$/$Ni_3V_2O_8$ electrodes demonstrated an improved specific capacitance of 1734 F g^{-1} at 1 A g^{-1}, with 96% of the initial capacitance retained after 8000 cycles.[15] Formation of various nanostructures has a high influence on supercapacitor behavior, whose structures are attained by varying the synthesis method.[16]

Carbon is the most commonly utilized component material, and it has garnered significant interest because of its high electronic conductivity, large specific surface area, controllable pore size, excellent chemical stability, and good mechanical strength.[17] Carbon is classified into two types: graphitic and nongraphitic carbon. Graphene is a 2D material that can be exfoliated from graphite with a closely packed conjugated hexagonal lattice.[18] It has some special properties beneficial for electronic devices such as high electrical conductivity, charge-carrier mobility, good transparency, high mechanical strength, and inherent flexibility. Graphene has a high specific surface area like other 2D materials, which is most suitable to maximize electrochemical active sites.[17] However, the preparation of single-layer graphene is cost-effective and difficult.[19] The typical reduced graphene oxide (RGO) replaces graphene. It features a large conjugated aromatic ring structure akin to that of graphene, allowing for physical interactions with porous carbon materials. Additionally, its numerous functional groups enable chemical interactions with conducting polymers, facilitating the development of solid-state devices for supercapacitor applications.[20−23] The network structure of the RGO provides more active sites for redox reactions. Consequently, the Ni$_2$V$_2$O7 and rGO@Ni$_2$V$_2$O7 nanorods demonstrate the specific capacitances of 318 and 624 F g^{-1} at 1 A g^{-1}.[15] We are focusing on the enhancement in the electrochemical performance of $Ni_2V_2O_7$ with the rGO composite via tuning the nanostructure. The facile solvothermal method directs the complex structure formation by using a solvent such as ethylene glycol. The nanostructure without a capping agent is capable of increasing the capacitance and stability for the hybridization of pyrovanatate with the rGO solid-state supercapacitor.

In this study, the pristine NVO and NVO@rGO composites were successfully synthesized through the solvothermal process. The 3D crystalline NVO with a hollow nanosphere shape and 2D amorphous rGO with a sheet shape were successfully composited. The NVO@rGO 20-coated electrode showed high specific capacitance. For the device suitability in practical application, the liquid electrolyte and solid-state electrolyte devices were constructed with a negative (rGO) electrode and a positive (NVO@rGO 20) electrode. The device reveals its better suitability with high stability, reversibility, and high specific capacitance retention.

2. EXPERIMENTAL SECTION

2.1. Materials and Reagents. All chemical reagents used in this experiment were of analytical grade and used as received without additional purification: nickel nitrate hexahydrate ($Ni(NO_3)\cdot 6H_2O$, 99.99%), ammonium metavanadate (NH_4VO_3, 98%), ethylene glycol ($C_2H_6O_2$), sulfuric acid (H_2SO_4, 98%), phosphoric acid (H_3PO_4, 99.9%), graphite fine powder (99.99%), potassium permanganate ($KMnO_4$, 99.9%), hydrogen peroxide (H_2O_2, 30 wt %), polyvinylidene difluoride (PVDF, 99%), acetylene black, *N*-methyl-2-pyrrolidone (NMP), and potassium hydroxide (KOH, 99%).

2.2. Hollow-Sphere $Ni_2V_2O_7$-Encapsulated rGO Nanosheet Preparation through a Facile Solvothermal Route. A 10 mmol portion of nickel nitrate hexahydrate ($Ni(NO_3)_2\cdot 6H_2O$) was dissolved in 40 mL of ethylene glycol to create solution A, and 10 mmol of ammonium metavanadate (NH_4VO_3) was dissolved in 40 mL of ethylene glycol to create solution B. Each solution was stirred separately for 15 min, with solution B being stirred at 80 °C until it dissolved completely and turned pale yellow. After solution B cooled to room temperature, it was mixed with solution A and stirred for 15 min. The resulting mixture was transferred to a 100 mL Teflon-lined autoclave and maintained at 180 °C for 24 h. After the reaction, the mixture was brought to room temperature, centrifuged several times with water and ethanol, and dried for 24 h at 60 °C. The resulting powder was then calcined at 450 °C for 4 h. The rGO preparation was carried out using a modified Hummer's method, following the synthesis procedure outlined in a previous report.[24] A similar

https://doi.org/10.1021/acsomega.4c08731
ACS Omega 2024, 9, 51481−51493

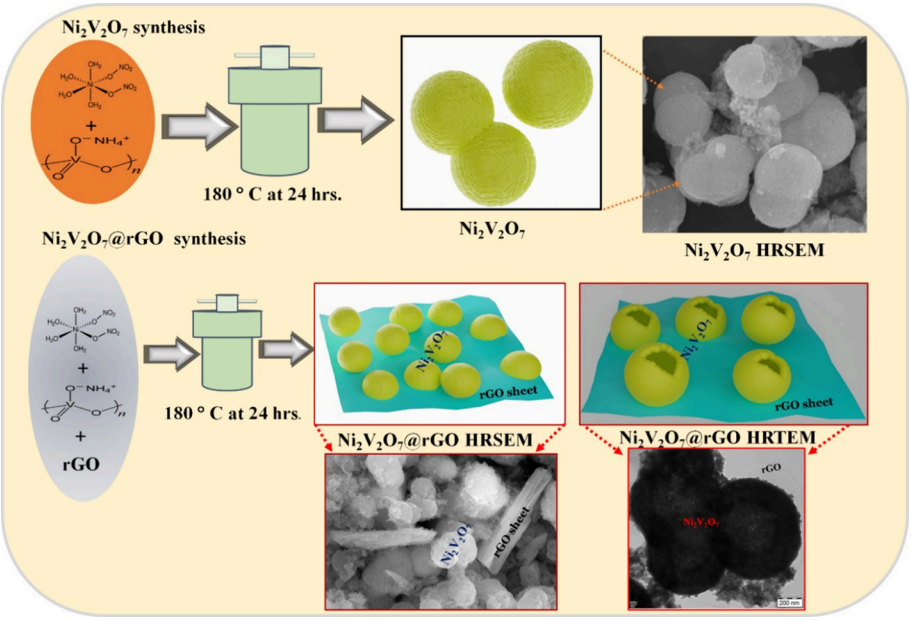

Figure 1. Schematic diagram of the NVO and NVO@rGO synthesis procedures.

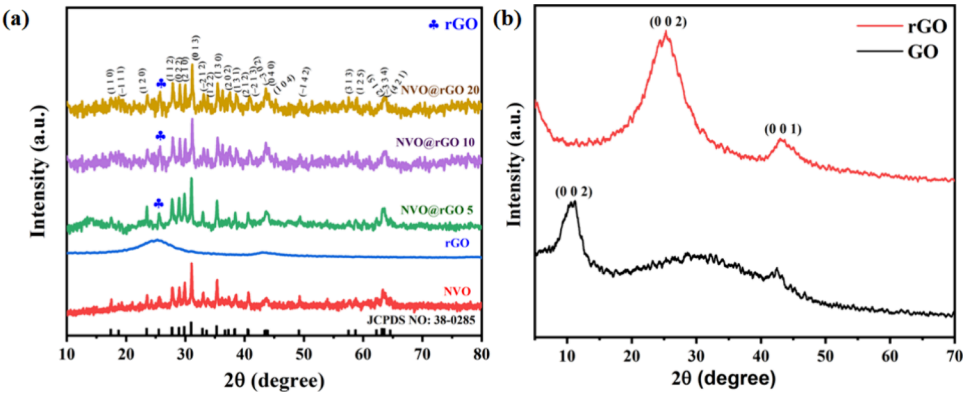

Figure 2. XRD patterns of (a) NVO and NVO@rGO, and (b) as-synthesized GO and rGO.

procedure was followed for $Ni_2V_2O_7$ with the rGO composite, with the addition of different weights of rGO such as 5, 10, and 20 mg, and named pristine NVO, NVO@rGO 5, NVO@rGO 10, and NVO@rGO 20, respectively. A schematic representation of the synthesis process of NVO and the NVO@rGO composite is shown in Figure 1.

2.3. Gel Electrolyte Synthesis. 1 g of KOH was dissolved in 20 mL of water for 10 min under continuous stirring. Subsequently, PVA was added to the solution and kept at 80 °C for 4 h to form a gel and dried in a vacuum oven for 12 h.

3. RESULTS AND DISCUSSION

3.1. Structural Analysis. An XRD diffraction pattern was obtained for the synthesized materials, as shown in Figure 2a. The pattern reveals the monoclinic structure with a space group of *P*21/*c*. The lattice parameters *a*, *b*, and *c* have values of 6.5150, 8.3030, and 9.350 Å, respectively. From the observation of the main peak position in the order of NVO < NVO@rGO 5 < NVO@rGO 10 < NVO@rGO 20 at 31.0289, 31.0413, 31.138, and 31.1615°, the shifting toward the higher-angle side of materials NVO@rGO 10 and NVO@rGO 20 is indicated, as compared to the pristine peak. Table S1 lists the parameter calculated from the XRD pattern. The FWHM value indicates the peak broadening in NVO@rGO 5 than pristine. From the concept of shifting toward a higher-angle side and peak broadening, the samples, NVO@rGO 5, NVO@rGO 10, and NVO@rGO 20 are under a compressive strain due to the induced strain by the rGO composite. The interplanar distance of materials was calculated by using Bragg's diffraction equation and its dependency with peak position; the material NVO@rGO 5 had a high *d*-spacing. The crystallite size of the materials was calculated by using the Scherrer formula.[25] The incorporation of rGO into the material decreased the crystallite size randomly. However, the decreasing crystallite size was attained by dislocations in the lattices, followed by the induced compressive strain on the lattice.[22] The large dislocations induced the large strain, which causes the attainment of minimum crystallite size in NVO@rGO 10. Figure 2b shows the XRD patterns of GO and rGO; upon reduction of oxygen, the peak shifted to a higher-angle side, showing the formation of rGO. The broad peak shape of GO and rGO indicates the amorphous nature of the carbon material.

Raman spectrum analysis is a tool used to conform the crystal structure as prepared. The nickel vanadate and amorphous formation of rGO in the range of 100−2000

https://doi.org/10.1021/acsomega.4c08731
ACS Omega 2024, 9, 51481−51493

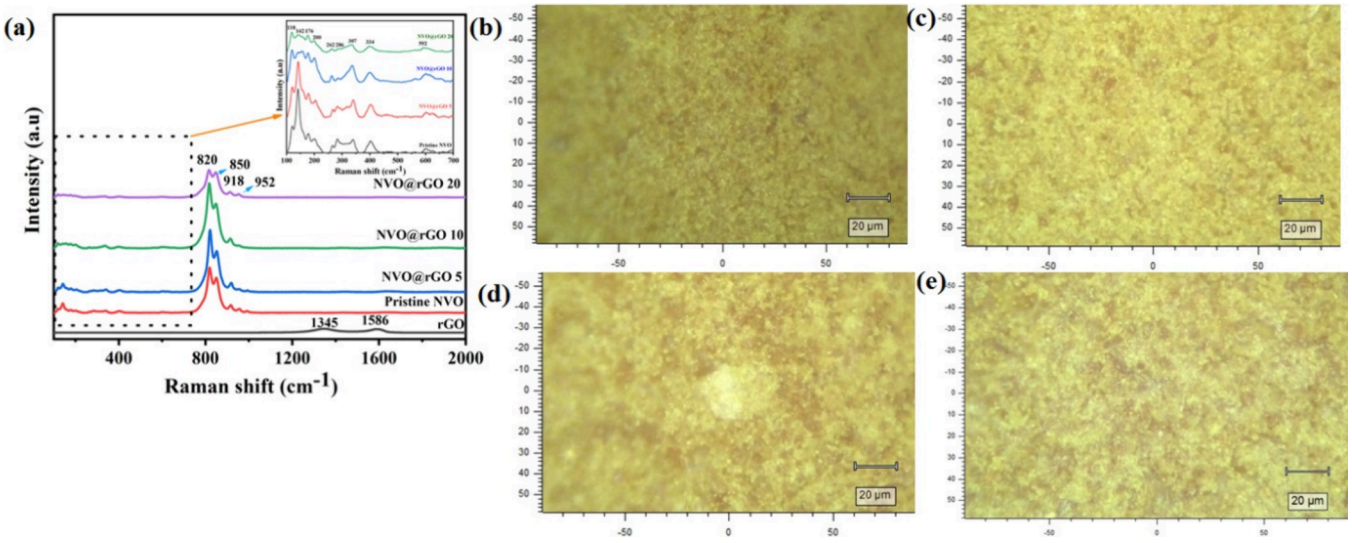

Figure 3. Shows the Raman spectrum of (a) NVO and rGO composites and the samples where the Raman analysis is taken. (b) NVO, (c) NVO@rGO 5, (d) NVO@rGO 10, and (e) NVO@rGO 20.

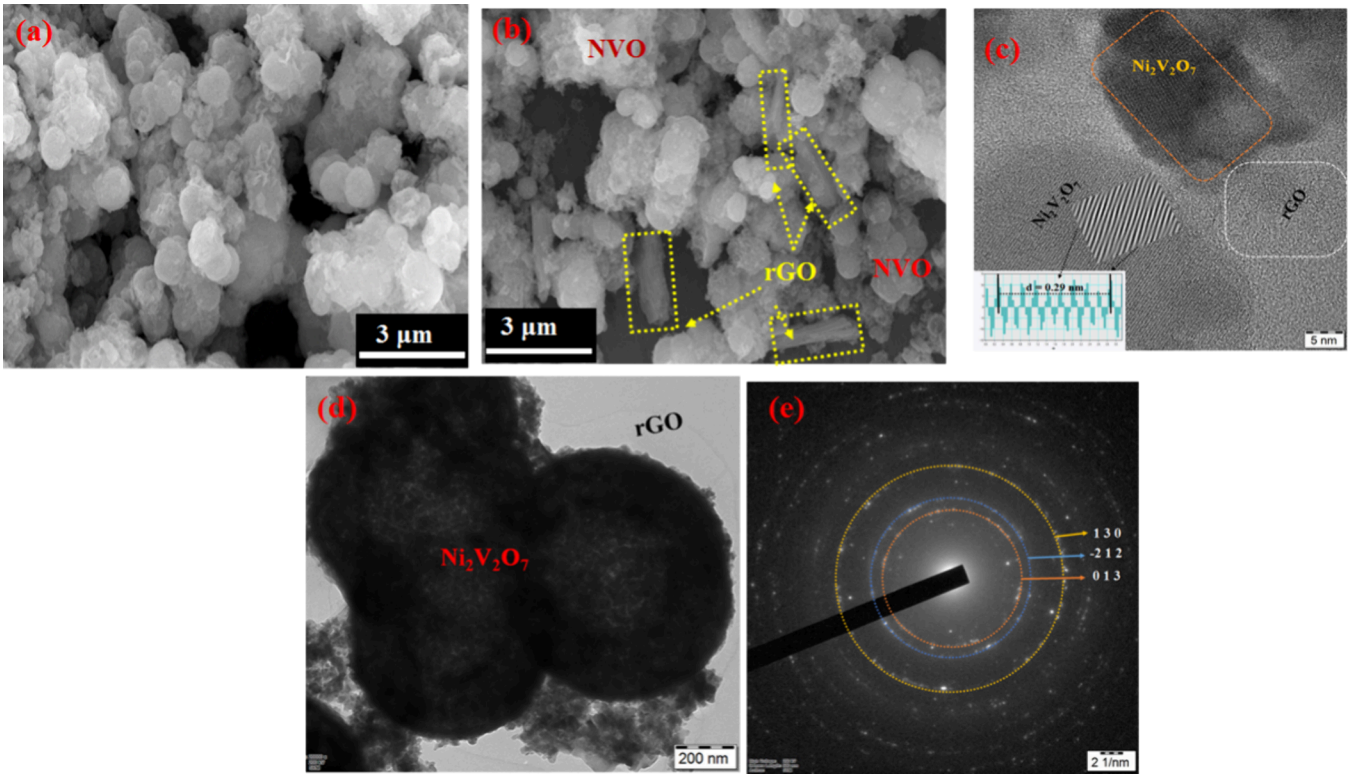

Figure 4. (a) HRSEM morphology of NVO, (b) HRSEM morphology of NVO@rGO 20, (c, d) HRTEM image morphology of the NVO@rGO 20 composite, and (e) SAED pattern of polycrystalline NVO.

cm^{-1} is shown in Figure 3a. The presence of peaks at 118, 142, 176, 200, 262, 286, 307, 334, 592, 820, 850, 918, and 952 cm^{-1} indicates the formation of NVO. The peaks at 200, 262, 334, 592, and 918 cm^{-1} are ascribed to Ni−O.[26,27] The peaks at 142, 286, 820, 850, and 952 are assigned to the V−O vibrations.[28,29] The rGO peaks at 1345 and 1586 cm^{-1} are the prominent peaks of the D and G bands, respectively. The D band originates from the breathing modes of sp^2 carbon atoms in rings and is triggered by defects and disorder in the graphene lattice. A higher D band intensity indicates more defects and disorder. The G band corresponds to the in-plane stretching vibration of sp^2 carbon atoms. The intensity ratio (I_D/I_G) of the peak value is 0.84; the ratio value indicates a higher level of defects and disorder in RGO.[30,31] The samples where the Raman spectrum is observed are shown in Figure 3b−e.

3.2. Surface Morphology Analysis. The surface morphology of synthesized materials is analyzed through high-resolution scanning electron microscopy (HRSEM) and high-resolution transmission electron microscopy (HRTEM), shown in Figure 4. The template-free solvothermal synthesis route using ethylene glycol as a solvent forms the

https://doi.org/10.1021/acsomega.4c08731
ACS Omega 2024, 9, 51481−51493

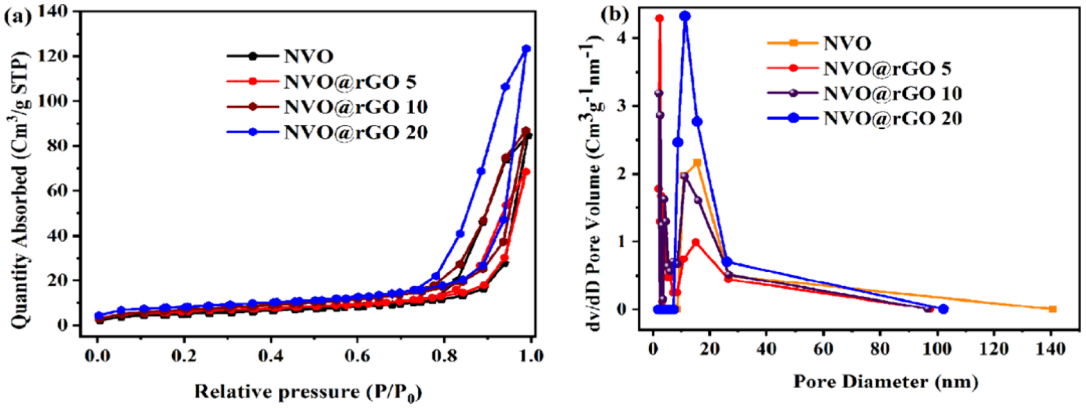

Figure 5. (a) BET isotherm adsorption−desorption curve of the synthesized samples and (b) pore diameter of the synthesized samples.

nanostructure of NVO, as shown in Figure 4a. Here, ethylene glycol directs the NVO structure formation to a hollow nanosphere by self-assembling the Ni and V precursors. The formation of the hollow nanosphere started with small particles, and the growth extended as nanoflakes. The flakes are aggregated like flakey-on-flakey network structures and form the hollow nanosphere.[32,33] The rGO sheets are assembled one on another by Vander waals interaction. On the composite, the NVO hollow nanospheres are partially encapsulated on the rGO surface. Figure S1a shows the NVO@rGO 5 nanostructure and the hollow shape of NVO clearly observed inside the dotted region. Figure S1b shows the NVO@rGO 10 nanostructure and the presence of rGO and NVO observed in the morphology. Figure 4b shows the NVO@rGO 20 nanostructure with NVO and rGO. The increasing rGO concentration increases the 2D surface of rGO in NVO@rGO 10 and NVO@rGO 20. The 3D hollow nanosphere and the 2D rGO surface increase the outer surface area, which is capable of increasing the reaction with other particle. Figure S1c shows the 2D surface of rGO in HRSEM.

HRTEM resembles the actual shape of samples, as shown in Figure 4c,d. HRTEM reveals the hollow nanosphere shape by aggregation of NVO nanoflakes, and the void space of the hollow is clearly observed to be dark in color on the outer curved surface and the bottom of the hollow nanosphere as light in color, shown in the image. The rGO presence with a sheet-like morphology and the NVO hollow nanospheres are distributed partially on the surface of rGO. The calculated *d*-spacing value lies between 0.3 and 0.29 nm for the NVO polycrystalline structure. Figure 4e shows the selective area electron diffraction pattern and reveals the respective *hkl* indices of [130] and [−212] along with identified high-intensity peak plane [013] in XRD.

3.3. Energy-Dispersive X-ray (EDX) Analysis. Figure S2 reveals the EDX analysis of the samples. The samples contain elements such as Ni, V, and O in pristine NVO, while in rGO-anchored NVO, the elements Ni, V, O, and C are presented.

3.4. Surface Analysis. The specific surface area was measured using a Brunauer−Emmett−Teller (BET) instrument. According to IUPAC classification, the isotherm adsorption−desorption curve of the synthesized materials indicates a type IV behavior, as observed in Figure 5a. The pore diameter of the synthesized materials and the mesoporous nature of the surface are observed in Figure 5b. The BET surface area was analyzed through a multipoint BET measurement. The specific surface area of the synthesized samples shows the increment in the order of NVO < NVO@rGO 5 < NVO@rGO 10 < NVO@rGO 20; it reveals a clear dependency to the added rGO, as shown in Table 1. The

Table 1. Parameters Calculated from BET Analysis

material	specific surface area(m^2/g)	pore diameter (nm)	pore volume (cc/g)	type
NVO	18.336	15.540	0.139	type IV
NVO@rGO 5	21.430	15.060	0.107	type IV
NVO@rGO 10	25.232	15.917	0.139	type IV
NVO@rGO 20	29.034	11.296	0.204	type IV

measurement indicates that the added rGO increases the specific surface area more than the pristine NVO. However, the increasing rGO by fixing the NVO concentration indicates the increasing specific surface area. Meanwhile, the NVO covered area on the 2D surface decreases upon increasing the rGO concentration. Thereby, the high specific area was obtained due to the maximum concentration of rGO in NVO@rGO 20, which is about 63% higher than the pristine NVO.

3.5. X-ray Photoelectron Spectroscopy. The survey spectrum of NVO@rGO reveals the composition in the samples such as Ni and V Figure 6a. Three sharp peaks in the spectrum are attributed to Ni 2p, V 2p, O 1s, and C 1s. The Ni 2p spectrum has spin−orbit splitting states of $2p_{3/2}$ and $2p_{1/2}$, as shown in Figure 6b. The Ni 2p peak demonstrates mixed oxidation states of +2 and +3 and the satellite peak tailed after Ni $2p_{3/2}$ and $2p_{1/2}$. Ni^{2+} presents with binding energies of 856 and 873.5 eV for the spin orbit splitting states of $2p_{3/2}$ and $2p_{1/2}$, respectively.[15] The energy difference between these two states is 17.61 eV. The binding energies of 857.3 and 874.8 eV are observed for Ni^{3+} for the spin−orbit splitting states of $2p_{3/2}$ and $2p_{1/2}$, respectively. The energy difference between these two states is 17.43 eV. Figure 6c depicts the spectrum of V 2p with spin−orbit splitting states of $2p_{3/2}$ and $2p_{1/2}$. The oxidation states of +4 and +5 are observed in the deconvolution spectrum with respective binding energies. V^{4+} split with binding energies of 517.17 and 524.1 eV for respective spin−orbit splitting states $2p_{3/2}$ and $2p_{1/2}$. V^{5+} split with binding energies of 518 and 525.2 eV for the spin−orbit splitting states of $2p_{3/2}$ and $2p_{1/2}$, respectively.[16] The energy

https://doi.org/10.1021/acsomega.4c08731
ACS Omega 2024, 9, 51481−51493

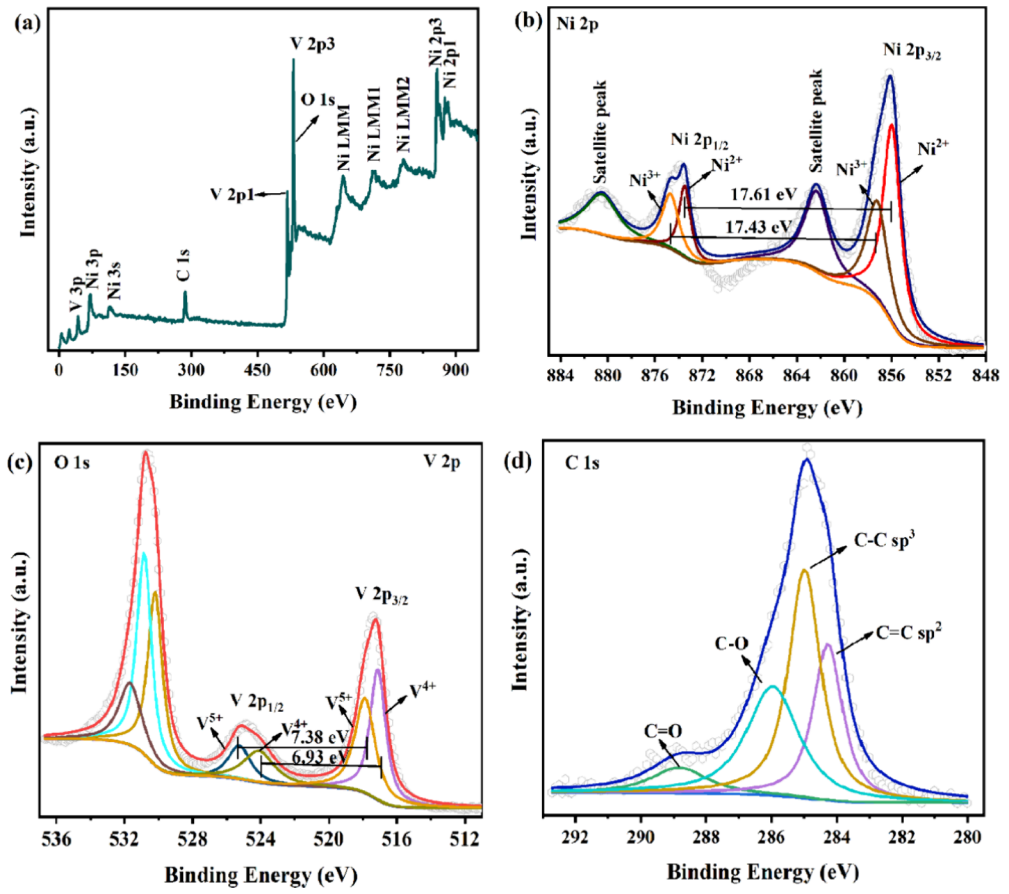

Figure 6. (a) XPS survey spectrum of NVO@rGO 20. (b) XPS spectra of Ni 2p, (c) XPS spectra of V 2p and O 1s. (d) XPS spectra of C 1s.

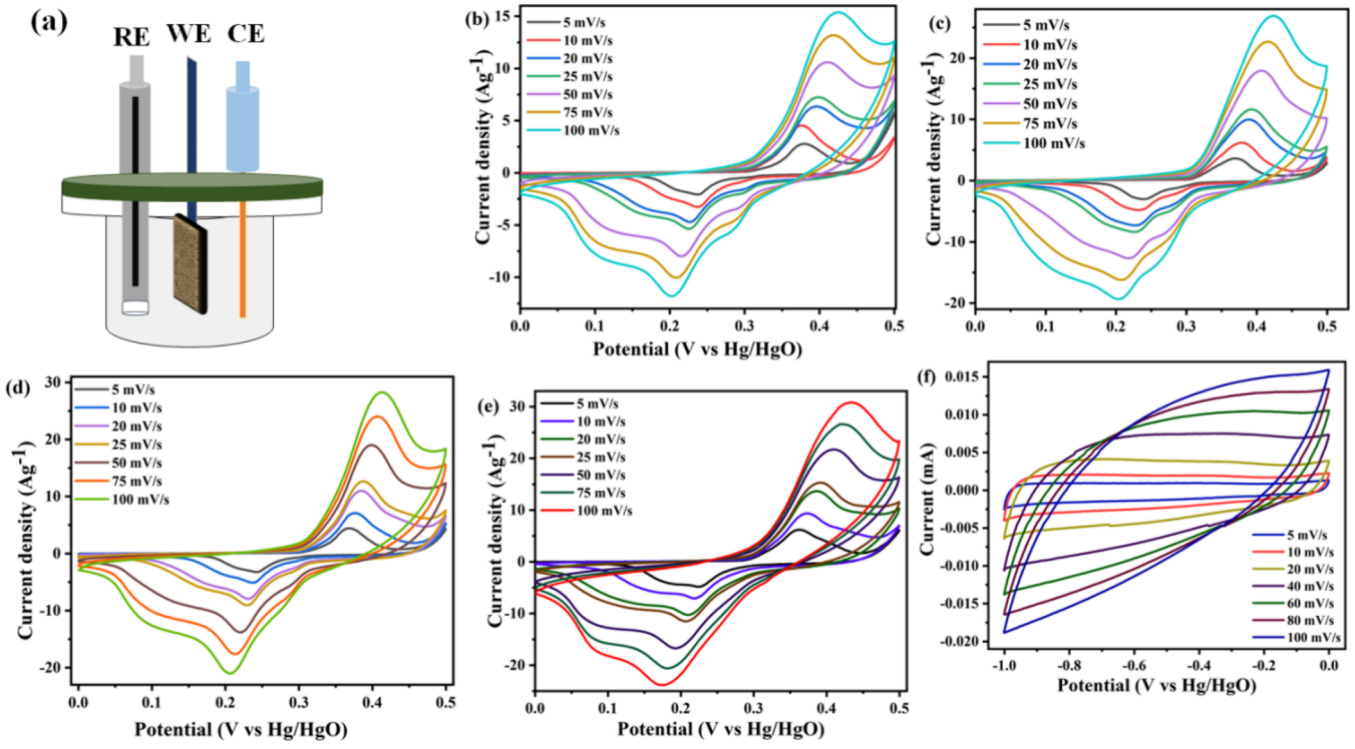

Figure 7. (a) Pictorial representation of a three-electrode system. (b) CV graph of NVO. (c) CV graph of NVO@rGO 5. (d) CV graph of NVO@rGO 10. (e) CV graph of NVO@rGO 20. (f) CV graph of rGO.

https://doi.org/10.1021/acsomega.4c08731
ACS Omega 2024, 9, 51481−51493

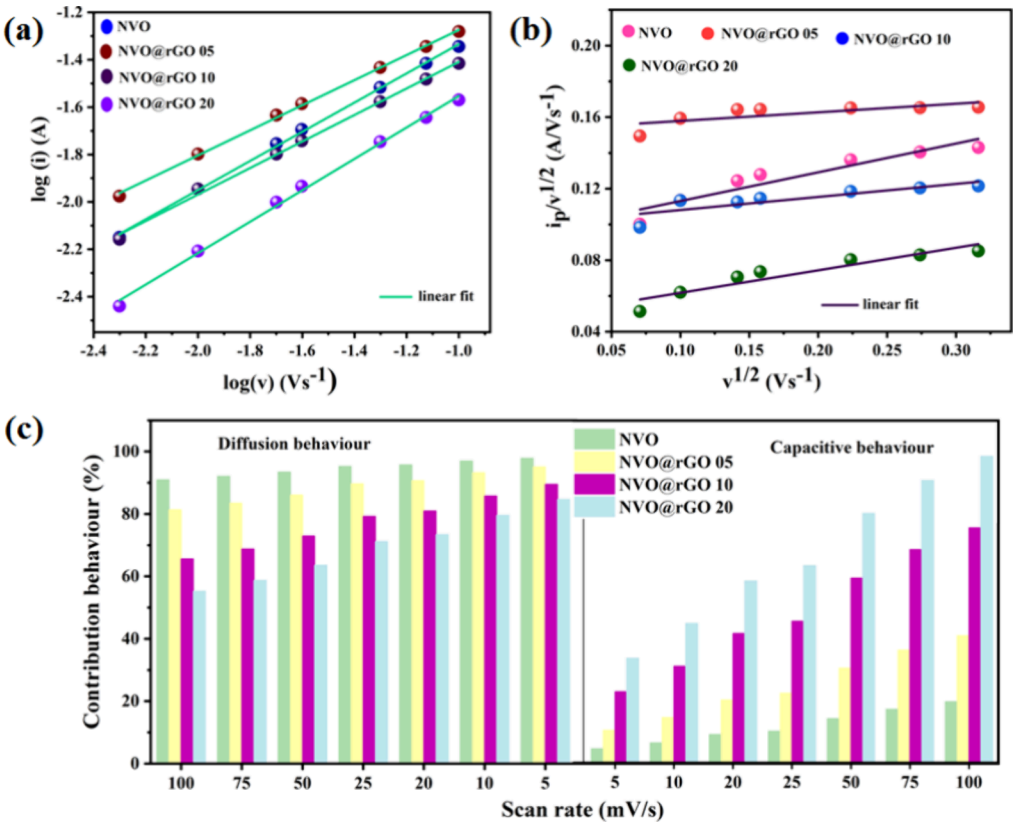

Figure 8. (a) Linear plot of log(v) vs log(i), (b) $v^{1/2}$ vs i_p/ $v^{1/2}$, and (c) contribution percentages of capacitive and diffusive percentage in NVO, NVO@rGO 5, NVO@rGO 10, and NVO@rGO 20.

differences between $2p_{3/2}$ and $2p_{1/2}$ states are 6.93 and 7.38 eV for V^{4+} and V^{5+}, respectively. O 1s has three characteristic peaks due to its presence with various bonds. The peak at 530.2 eV indicates the lattice oxygen, which is attributed to Ni−O and V−O. A peak at a binding energy of 530.9 eV indicates the adsorbed oxygen, which contains a hydroxyl group from the water molecule. Another peak at 531.8 eV is attributed to O−C═O, which indicates the presence of rGO. Four peaks are observed from the high resolution of the C 1s spectrum, as shown in Figure 6d. The peaks are located at binding energies of 288.9, 286, 285.9, and 284.3 eV, which corresponds to the bonds C═O, C−O, C−C sp^3 hybridization, and C═C sp^2 hybridization, respectively.[34,35]

3.6. Electrochemical Studies. From the GCD graph, the specific capacitance, C_{sp} (F g^{-1}), was calculated using eq 1

$$C_{sp} = \frac{I \times \Delta t}{m \times \Delta V} \tag{1}$$

where I, Δt, m, and ΔV represent the constant discharge current (A), the area under the discharge curve (s), the mass of the active materials (g), and the potential window (V), respectively. The following mass-balancing method as in eq 2 was used to optimize the positive electrode and negative electrode materials.

$$\frac{m^+}{m^-} = \frac{C^- \times \Delta V^-}{q^+} \tag{2}$$

where m^+ and m^- represent the masses of the positive electrode (NVO@rGO) and negative electrode (rGO) materials, respectively, C^- and ΔV^- are the specific capacitance (C_{sp}) and potential window of the negative electrode, and q^+ denotes the specific capacity (C_{sp}) of the positive electrode. For hybrid supercapacitors (SC), the mass ratio of positive and negative is 1:1.1, and the specific capacity (C_{GC}; mAh g^{-1}) was determined from the GCD curves, as shown in eq 3.

$$C_{GC} = \frac{I \times \Delta t}{m \times 3.6} \tag{3}$$

where I is the constant discharge current (A), Δt is the discharging time (s), and m is the mass of the active electrode materials in grams.

The specific energy (E_d) and specific power (P_d) of the hybrid supercapacitor were calculated using eqs 4 and 5:

$$E_d = \frac{I \times v(t)\mathrm{d}t}{m \times 3.6} \tag{4}$$

$$P_d = \frac{E_d \times 3600}{\Delta t} \tag{5}$$

where E_d represents the energy density (Wh kg^{-1}), P_d denotes the power density (W kg^{-1}), $\int v(t)\mathrm{d}t$ is the integral of the GCD discharge area, m is the mass of active electrode materials (g), and Δt is the discharge time (s).[36]

As demonstrated in Figure 7a, the three-electrode system was combined with Hg/HgO as the reference electrode, Pt as the counter electrode, and synthesized material-coated Ni foam as the working electrode, which is the current collector, in KOH electrolyte. To prepare the aqueous basic electrolyte, 1 M KOH was stirred with 10 mL of DI water for 1 h. A Ni foam piece (1 cm × 1 cm) was washed with 3 mol of HCl, acetone, and ethanol and then dried. The mixture of the synthesized sample, carbon black, and NMP powder was taken

https://doi.org/10.1021/acsomega.4c08731
ACS Omega 2024, 9, 51481−51493

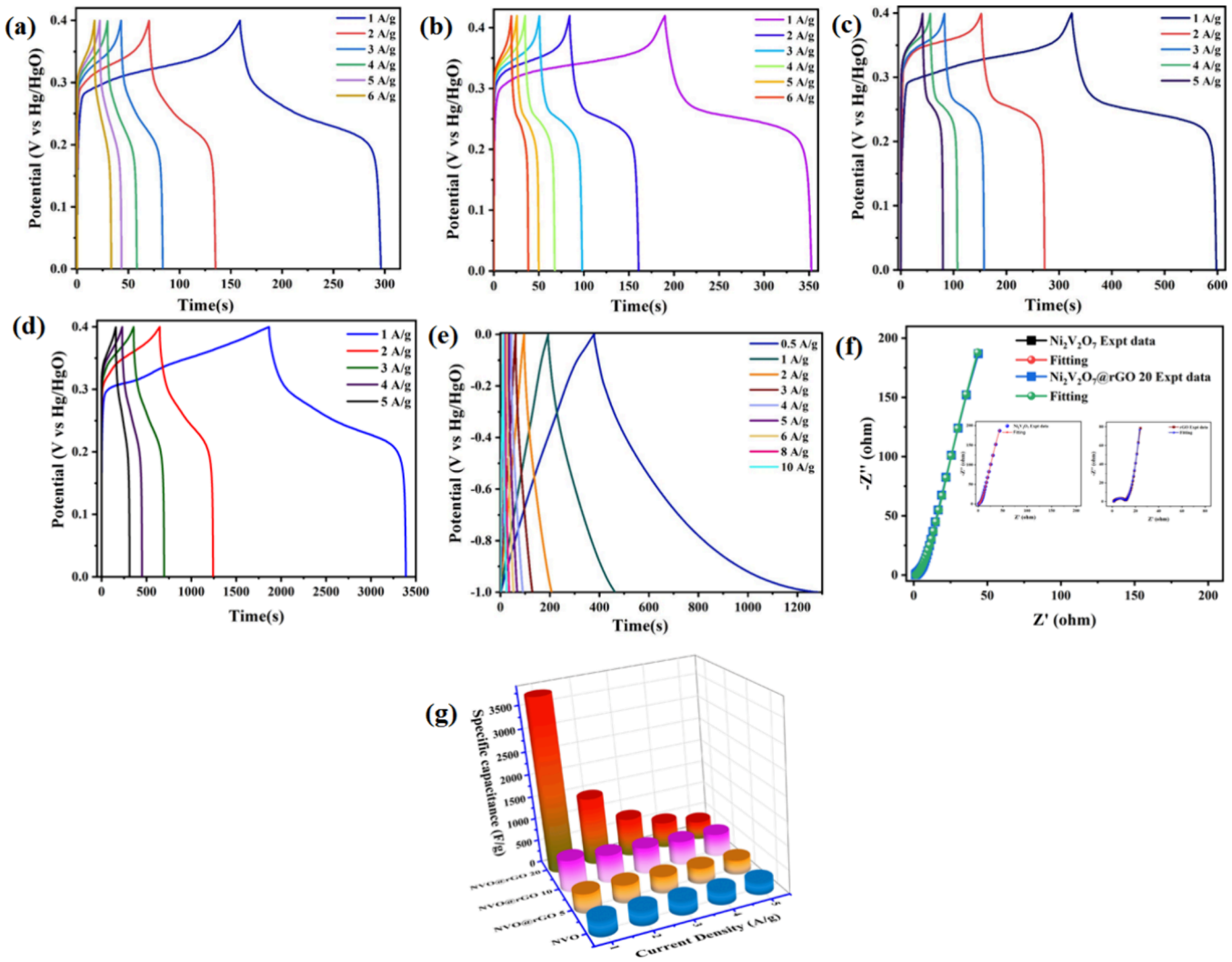

Figure 9. GCD graphs of (a) NVO, (b) NVO@rGO 05, (c) NVO@rGO 10, (d) NVO@rGO 20, and (e) rGO. (f) Nyquist plot with a solid symbol denoting experimental data and a solid line denoting fitted data. (g) Specific capacitance with increasing current density.

to form a paste and coated on Ni foam. This coated Ni foam was then dried at 60 °C for 24 h. The resulting electrode was then used to perform electrochemical characterization.

The CV curves for NVO, NVO@rGO 5, NVO@rGO 10, and NVO@rGO 20 at 5, 10, 20, 25, 50, 75, and 100 mV/s scan rates are observed in Figure 7b−e. The activation of the working electrode proceeded at a scan rate of 25 mV/s and a fixed potential window between 0 and 0.5 V under 30 cycles. The CV graph shows the distinct oxidation and reduction peaks, the peak present in positive current indicates the phenomena of oxidation, and the peak present in negative current indicates the phenomena of reduction. The pattern of CV graph and the oxidation and reduction process resembles the battery-type capacitive behavior. The voltammogram displays symmetric Faradaic redox peaks between 0 and 0.5 V (vs Hg/HgO), indicating that energy storage is facilitated by both the rapid diffusion of OH^- ions at the electrode surface and the predominant Faradaic redox reactions of NVO. In the process of oxidation, NVO converts into VO_4 and NiOOH and reverts to NVO upon discharge during the electrochemical cycle. At 5 mV/s, ions are getting enough time to undergo a diffusion process owing to high specific capacitance. An increase in the scan rate results in a corresponding rise in the peak current (i_p). Notably, the reduction and oxidation peak shape emerges up to a scan rate 100 mV/s refers to the enhanced stability and reversibility of the synthesized NVO and NVO@rGO electrodes. The rGO-anchored NVO electrode exhibits superior cyclic stability up to higher scan rates, attributed to rGO's role in improving electrode conductivity to provide high specific capacitance. Furthermore, the NVO@rGO electrode demonstrates an increase in the area under the oxidation and reduction peaks than the NVO electrode, due to the intrinsic EDLC characteristics of rGO with more available active sites. The CV curve of rGO represents the EDLC behavior from a rectangular shape, with a large area, as shown in Figure 7f. Subsequently, the large integrated area in the graph provides the increased integrated area on the compositing material. As evident, the same was observed in the NVO@rGO CV curve, likely due to the presence of rGO. Subsequently, it enhances the active surface area and promotes faster ionic diffusion, thereby boosting electrochemical performance. The power law, defined by $i_p = a \times v^b$ where i_p represents the peak current (A) and v is the scan rate (mV/s), was utilized to compute the b value via the CV measurement. In this equation, a is a constant and b is an exponent constant of the power law. The determined b value

https://doi.org/10.1021/acsomega.4c08731
ACS Omega 2024, 9, 51481−51493

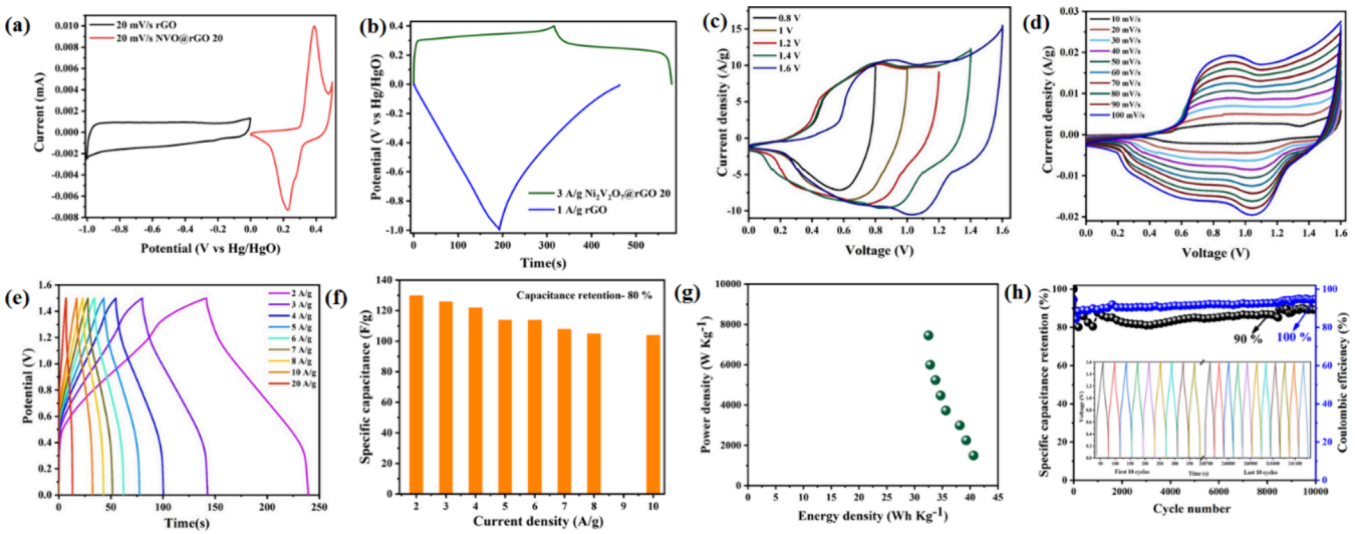

Figure 10. Liquid electrolyte device (a) CV graph for positive and negative electrodes, (b) GCD graph for positive and negative electrodes, (c) CV graph with different potential windows, (d) CV graph with different scan rates, (e) GCD graph with different current densities, (f) specific capacitance with different current densities, (g) power density and energy density of the fabricated device, and (h) stability of the hybrid supercapacitor with 10,000 cycles.

was used to evaluate the diffusion-controlled and capacitive-controlled percentages of electrode materials NVO, NVO@rGO 5, NVO@rGO 10, and NVO@rGO 20. $\log(i_p)$ vs $\log(V)$ was plotted to calculate the b value, as shown in Figure 8a. The linear fitting of the plot gives the b values. The computed b value was utilized to differentiate the way which type of mechanism was involved for charge storing. If the value is near 1, the electrode exhibits capacitive characteristics; if it is approximately 0.5, the charge storage process is controlled by diffusion. The respective samples of NVO, NVO@rGO 5, NVO@rGO 10, and NVO@rGO 20 have the b values of 0.52, 0.55, 0.61, and 0.66, respectively. The increasing rGO concentration increases the capacitive behavior more than NVO due to the adsorption and desorption for EDLC characteristics. The current response at a constant potential can be characterized by a combination of two distinct behaviors: one controlled by capacitance and the other by diffusion, shown in the following equations.

$$i_p = s_1\nu + s_2\nu^{1/2} \tag{6}$$

and

$$i_p/\nu^{1/2} = s_1\nu^{1/2} + s_2 \tag{7}$$

where s_1 and s_2 are constants and the peak current (i_p) is given by the sum of capacitive-controlled $(s_1\nu)$ and diffusion-controlled $(s_2\nu^{1/2})$ components.[24] The values of s_1 and s_2 were calculated from the linear fitting of eq 7, from Figure 8b. The slope of the equation gives the value of s_1, and the intercept is the value of s_2. The percentage of capacitive and diffusion-controlled process is shown in Figure 8c. Where the scan rate is higher, the diffusion-controlled process is maximum for all the materials. On rGO-anchored NVO, the capacitive behavior is enhanced due to the increased active surface area by the increased 2D surface area. The high capacitive percentage of 44.78% is obtained in NVO@rGO 20 at a scan rate of 100 mV/s; thereby, the material has high active sites.

The electrochemical performance was further studied to calculate specific capacitance and electrochemical stability of prepared electrodes. The setup was run under a fixed potential of 0−0.4 V. Figure 9a−d represents the GCD graph of NVO and NVO@rGO with different concentrations at different current densities. The 0 to 0.4 V in the curve indicates the oxidation and reduction from 0.4 to 0 V. Furthermore, the discharge time for the rGO-coated electrode is high due to the more available active sites. The nature of the charge and discharge mechanism refers to the battery-type capacitor behavior. The rGO charge and discharge mechanism possesses the EDLC behavior, as observed from Figure 9e. Electrochemical impedance spectroscopy data were recorded in the frequency range between 100 kHz and 0.01 Hz and fitted with the $R-C$ circuit. Figure 9f shows the Nyquist plot, and the intercept in the x-axis indicates the solution resistance (R_s) in all samples. rGO has small a semicircle, suggesting the faster charge transfer between electrolytes and electrodes. The linear plot in NVO that changed and started with a small semicircle indicates the influence of rGO in ion diffusion in NVO@rGO 20. The R_s value is 1.442Ω and the R_{ct} value is 4.213 Ω found from the radius of the semicircle in the high-frequency range, suggesting that the charge transfer mechanism happens between the electrode and electrolyte, and the linear slope of the plot in the low-frequency region indicates the ion diffusion, described by the Warburg impedance.[37] The calculated specific capacitance value for NVO is 343.3 F g^{-1} at 1 A g^{-1}, and it increases with increasing rGO composition percentage. The selected composite possesses great influence in electrochemical performance evidenced by the enhancement in specific capacitance, as shown in Figure 9g. NVO@rGO 5, NVO@rGO 10, and NVO@rGO 20 show specific capacitances of 406, 684, and 3807 F g^{-1} at 1 A g^{-1}, respectively. The increased 2D specific surface area, due to the increment in the rGO concentration by keeping NVO as a fixed concentration, increases the active surface area for electrochemical performance. Furthermore, the hydroxyl functional group in rGO undergoes the redox process. Similarly, the redox curve in GCD even increases the current density, which indicates the good reversibility of electrodes. Here, the synthesized material crosses the specific capacitance value of the Ni_2V_2O7 nanorod

https://doi.org/10.1021/acsomega.4c08731
ACS Omega 2024, 9, 51481−51493

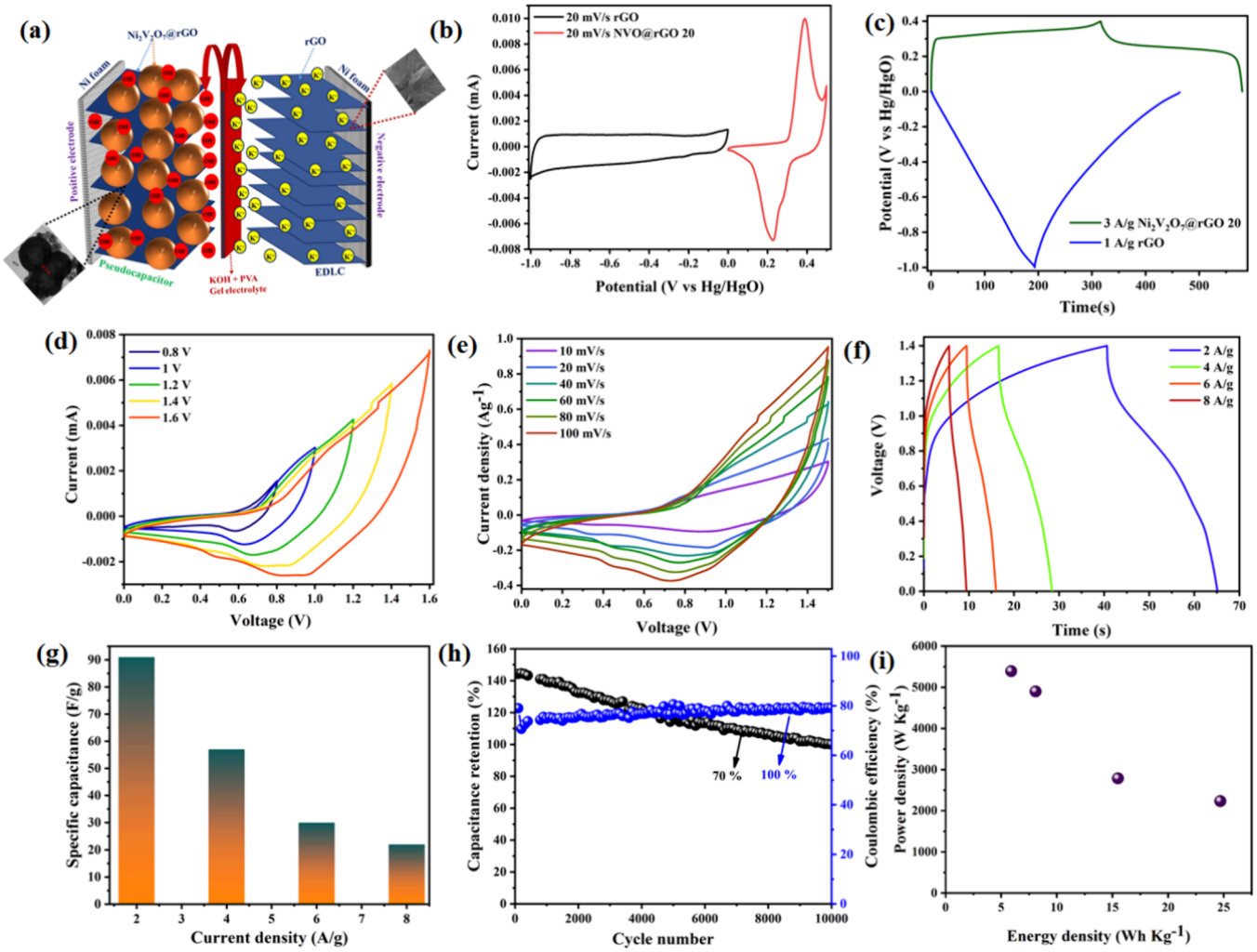

Figure 11. Solid-state device (a) demonstration of device setup and charge transfer mechanism, (b) CV graph of different electrodes, (c) GCD graph of positive and negative electrodes, (d) CV graph with different potential windows, (e) CV graph with different scan rates, (f) GCD graph with different current densities, (g) specific capacitance with different current densities, (h) stability of the hybrid supercapacitor with 10,000 cycles, and (i) power density and energy density of the solid-state device at different current densities.

(318 F g^{-1}) and the Ni_2V_2O7 nanorod@rGO (624 F g^{-1}) at 1 A g^{-1}, which is reported by Palani et al.[38] The improvement is likely due to the increased number of active sites on the 3D hollow nanosphere.

The device was fabricated with liquid electrolyte by keeping rGO as the negative electrode, NVO@rGO as the positive electrode, and 1 M KOH liquid electrolyte. Figure 10a shows the CV graph of rGO in EDLC behavior; the potential window on the left side between −1 and 0 V indicates that the electrode works under a negative potential window and the NVO@rGO curve on the right side with a potential window between 0 and 0.5 V works as a positive electrode. The GCD graph and the charging and discharging mechanism of the created positive and negative electrodes are shown in Figure 10b. The nature of the GCD curve for the positive electrode resembles the battery-type capacitor behavior, and the negative electrode resembles the EDLC behavior. The voltage versus current graph indicates the mixed battery type (redox) behavior and the EDLC behavior known, as the hybrid supercapacitor, as shown in Figure 10c. With increasing potential window, the hybrid supercapacitor curve does not show any distortions, which shows the device withstanding the hybrid supercapacitor behavior up to 1.6 V. Figure 10d shows the scan rate variation from 10 to 100 mV/s by keeping a fixed potential window of 1.5 V. The curve reveals the quasi-rectangular shape of the hybrid supercapacitor behavior, and the integrated area increased with increasing scan rate. The GCD graph slightly differed from the three-electrode system, which indicates the contribution of negative electrode rGO with EDLC behavior for hybrid supercapacitor devices, as shown in Figure 10e. The GCD profiles are nonlinear in shape and have a very low IR drop, indicating that the device performed well during charging and discharging. The plot between current density and specific capacitance refers to 80% of capacitance retention with current density, as shown in Figure 10f. The specific capacitance value is 130 F g^{-1} at a flow rate of 2 A g^{-1}. The excellent cyclic stability was identified by running 10,000 cycles, as shown in Figure 10g. The specific capacitance retention of 90% even after 10,000 cycles refers to this device for practical application. The excellent cyclic stability was attained due to the rGO presence in NVO@rGO composition. NVO is a type II material in terms of cyclic stability. Generally, type II materials' specific capacitance retention is lower than 100% after the self-activation process.[39] However, carbon-based rGO belongs to the type I material, which has 100% specific capacitance retention even with the

https://doi.org/10.1021/acsomega.4c08731
ACS Omega 2024, 9, 51481−51493

Table 2. Comparison Table with Morphology and Parameters Calculated from Electrochemical Studies

material	morphology	specific capacitance	specific capacitance retention	power density(W/kg)	energy density (Wh/kg)	ref.
$Ni_2V_2O_7$	nanorods	894 F g^{-1} at 0.4 mA/cm^2 (1 M KOH)				13
$Ni_2V_2O_7$	microsphere	959 F g^{-1} at 5 mA g^{-1} (1 M KOH)				40
$Ni_2V_2O_7$	nanorods	318 F g^{-1} at 1 A g^{-1} (1 M KOH)				38
$Ni_2V_2O_7$@rGO 10	nanorods on sheets	624 F g^{-1} at 1 A g^{-1} (1 M KOH)	95% after 1000 cycles	771	22.28	
NVO@rGO 20	hollow nanosphere on sheets	3807 F g^{-1} at 1 A g^{-1} (1 M KOH)				this work
NVO@rGO 20//rGO	hollow nanosphere on sheets for positive electrode, and sheets for negative electrode	91 F g^{-1} at 1 A g^{-1} (KOH + PVA gel electrolyte)	70% after 10,000 cycles	33	7467	

higher scan rate. The excellent cyclic stability of this type I material comes from the mechanism of the charge and discharge process in the same material. The ions are reversibly adsorbed and desorbed on the active sites of the rGO material. So, the specific capacitance retention of the rGO-anchored material shows higher cyclic stability than the pristine NVO.[17] The obtained Coulombic efficiency is even more advantageous for large-scale industrial applications. The inserted graph refers to the hybrid supercapacitor charge−discharge curve taken from first and last 10 cycles, indicating the successive charging and discharging processes over 10,000 cycles. Thereby, this device reveals its long life and excellent reversibility for electrochemical performance. The power density and energy density calculated at different current densities are shown in Figure 10h. The power density was 1000 to 8000 W kg^{-1}, and the energy density was found between 30 and 43 Wh kg^{-1}.

The solid-state device was constructed with rGO as a negative electrode, NVO@rGO as a positive electrode, and KOH gel electrolyte. Figure 11a shows the demonstration of the construction of the solid-state device and the charge transfer mechanism. The device was sandwiched in the horizontal direction, starting from left to right: the positive electrode on the left side, the gel electrolyte in the middle, and the negative electrode on the right side. The electrodes' electrochemical response was identified before conducting electrochemical studies, the positive electrode behavior of NVO@rGO 20 and the negative electrode behavior of rGO, observed in Figure 11b. The charging and discharging mechanism of electrodes refers to the battery-type capacitive behavior of NVO@rGO 20 and the EDLC behavior of rGO observed from Figure 11c. In Figure 11d, the hybrid supercapacitor behavior was observed due to the quasi-rectangular-shaped CV curve. The voltage versus current graph was plotted to identify the stability of the device with a potential window. The stable hybrid supercapacitor curve is observed over the end potential of charging from 0.8 to 1.6 V. The optimum potential of 1.5 V is taken for further performance calculation, with the stability obtained up to 1.6 V. The potential window of 0 to 1.5 V was followed to analyze the CV performance with different scan rates, as shown in Figure 11e. With the observed CV area, the integrated area increases with the scan rate. The GCD curve reveals the hybrid supercapacitor behavior; the maximum discharge time of 65 s is observed for the current density of 2 A g^{-1}, as shown in Figure 11f. The successive charging and discharging process is observed with increasing different current densities, which indicates the stability over current density. The maximum specific capacitance of the hybrid supercapacitor was calculated at 2 A g^{-1} where we observed maximum discharging time as seen in Figure 11g. The Coulombic efficiency of 100% and the specific capacitance of 70% retained their initial capacity even after 10,000 cycles for scan rate 10 A g^{-1}, as shown in Figure 11h. The specific capacitance retention is lower in solid-state devices due to the air resistance created during the gel formation, which affects the ion flows. The power densities of 1500 to 6000 W kg^{-1} and energy densities of 5 to 25 Wh kg^{-1} were calculated for different current densities, as shown in Figure 11i. Finally, Table 2 shows the comparison between previous reports and our work; it clearly indicates the fabrication of the device in this particular composite and the electrochemical performance of this device with increased power density and energy density.

4. CONCLUSIONS

NVO pyrovanadate composited with amorphous rGO was successfully synthesized through a solvothermal process. The formation of NVO is guided by ethylene glycol, resulting in hollow nanospheres on the rGO surface. The composition of elements in the composite was identified through XPS. The BET-specific surface area calculation reveals the increasing specific surface area upon increasing rGO concentration. The 3D hollow sphere partially covered the 2D surface area of rGO. The active surface area increasing through increasing the specific surface area provides a high specific capacitance for NVO@rGO 20. The fabricated device for practical application shows the better electrochemical stability and reversibility over 10,000 cycles as expected. The specific capacitance retention of ∼90% for the liquid electrolyte device and ∼70% for the solid-state electrolyte device was obtained.

■ ASSOCIATED CONTENT

Supporting Information

The Supporting Information is available free of charge at https://pubs.acs.org/doi/10.1021/acsomega.4c08731.

Characterization details of NVO and rGO composite in different concentrations with NVO synthesized via the solvothermal process; lists of parameters calculated from XRD data; HRSEM morphological analysis; elemental mapping; and EDAX spectrum of NVO and rGO composite (PDF)

https://doi.org/10.1021/acsomega.4c08731
ACS Omega 2024, 9, 51481−51493

AUTHOR INFORMATION

Corresponding Author

Navamathavan Rangaswamy − *Department of Physics, School of Advanced Sciences, Vellore Institute of Technology (VIT) Chennai, Chennai 600127, India;* orcid.org/0000-0002-9185-6837; Email: navamathavan.r@vit.ac.in, navmath@yahoo.com

Author

Selvan Maruthasalamoorthy − *Department of Physics, School of Advanced Sciences, Vellore Institute of Technology (VIT) Chennai, Chennai 600127, India*

Complete contact information is available at: https://pubs.acs.org/10.1021/acsomega.4c08731

Notes

The authors declare no competing financial interest.

ACKNOWLEDGMENTS

The authors express their gratitude and appreciation to the VIT management for the support received throughout the completion of this research paper.

REFERENCES

(1) Liu, H.; Liu, X.; Wang, S.; Liu, H. K.; Li, L. Transition Metal Based Battery-Type Electrodes in Hybrid Supercapacitors: A Review. *Energy Storage Mater.* **2020**, *28*, 122−145.

(2) Augustyn, V.; Simon, P.; Dunn, B. Pseudocapacitive Oxide Materials for High-Rate Electrochemical Energy Storage. *Energy Environ. Sci.* **2014**, *7* (5), 1597−1614.

(3) Zhang, Y.; Jing, X.; Wang, Q.; Zheng, J.; Jiang, H.; Meng, C. Three-Dimensional Porous V_2O_5 Hierarchical Spheres as a Battery-Type Electrode for a Hybrid Supercapacitor with Excellent Charge Storage Performance. *Dalt. Trans.* **2017**, *46* (43), 15048−15058.

(4) Conway, B. E. Two-dimensional and quasi-two-dimensional isotherms for Li intercalation and upd processes at surfaces. *Electrochimica acta.* **1993**, *38* (9), 1249−1258.

(5) Herrero, E.; Buller, L. J.; Abruña, H. D. Underpotential Deposition at Single Crystal Surfaces of Au, Pt. *Ag and Other Materials. Chem. Rev.* **2001**, *101* (7), 1897−1930.

(6) Choi, C.; Ashby, D. S.; Butts, D. M.; DeBlock, R. H.; Wei, Q.; Lau, J.; Dunn, B. Achieving High Energy Density and High Power Density with Pseudocapacitive Materials. *Nat. Rev. Mater.* **2020**, *5* (1), 5−19.

(7) Rehder, D. The Future of/for Vanadium. *Dalt. Trans.* **2013**, *42* (33), 11749−11761.

(8) Yao, G.; Zhang, N.; Zhang, Y.; Zhou, T. Nanostructured Transition Metal vanadates as Electrodes for Pseudo-Supercapacitors: A Review. *J. Nanoparticle Res.* **2021**, *23* (2), 1−27.

(9) Xia, D.; Gao, H.; Li, M.; Gong, F.; Li, M. Transition metal vanadates electrodes in lithium-ion batteries: A holistic review. *Energy Storage Mater.* **2021**, *35*, 169−191.

(10) Ni, S.; Liu, J.; Chao, D.; Mai, L. Vanadate-Based Materials for Li-Ion Batteries: The Search for Anodes for Practical Applications. *Adv. Energy Mater.* **2019**, *9* (14), 1−33.

(11) Anjass, M.; Lowe, G. A.; Streb, C. Molecular Vanadium Oxides for Energy Conversion and Energy Storage: Current Trends and Emerging Opportunities. *Angew. Chemie - Int. Ed.* **2021**, *60* (14), 7522−7532.

(12) Sun, Y. C.; Ouyang, Z. W.; Wang, J. F.; Wang, Z. X.; Xia, Z. C.; Rao, G. H. Breaking of 1D magnetism in a spin-1 chain antiferromagnet $Ni_2V_2O_7$: ESR and first-principles studies. *Eur. Phys. J. Plus* **2016**, 131.

(13) Ezhil Arasi, S.; Ranjithkumar, R.; Devendran, P.; Krishnakumar, M.; Arivarasan, A. Electrochemical Evaluation of Binary $Ni_2V_2O_7$ Nanorods as Pseudocapacitor Electrode Material. *Ceram. Int.* **2020**, *46* (14), 22709−22717.

(14) Subramanian, M. A.; Aravamudan, G.; Subba Rao, G. V. Oxide Pyrochlores - A Review. *Prog. Solid State Chem.* **1983**, *15* (2), 55−143.

(15) Palani, S.; Veerasamy, U. S.; Mona, Y.; Chaichana, C.; Suttakul, P.; Wanison, R. Facile Synthesis of RGO Nanosheet Encapsulated $Ni_2V_2O_7$ Nanorods for Energy Storage Applications. *Results Eng.* **2024**, *22*, No. 102134.

(16) Xia, D.; Wang, D.; Liu, W.; Gong, F. Rational Synthesis of "Grape-like" $Ni_2V_2O_7$ Microspheres as High-Capacity Anodes for Rechargeable Lithium Batteries. *Chem. - An Asian J.* **2021**, *16* (7), 775−782.

(17) Wu, Q.; He, T.; Zhang, Y.; Zhang, J.; Wang, Z.; Liu, Y.; Zhao, L.; Wu, Y.; Ran, F. Cyclic stability of supercapacitors: materials, energy storage mechanism, test methods, and device. *J. Mater. Chem. A* **2021**, *9* (43), 24094−24147.

(18) Stanford, M. G.; Rack, P. D.; Jariwala, D. Emerging nanofabrication and quantum confinement techniques for 2D materials beyond graphene. *npj 2D Mater. App.* **2018**, *2* (1), 20.

(19) Chee, W. K.; Lim, H. N.; Zainal, Z.; Huang, N. M.; Harrison, I.; Andou, Y. Flexible Graphene-Based Supercapacitors: A Review. *J. Phys. Chem. C* **2016**, *120* (8), 4153−4172.

(20) El-Kady, M. F.; Shao, Y.; Kaner, R. B. Graphene for Batteries, Supercapacitors and Beyond. *Nat. Rev. Mater.* **2016**, *1* (7), 1−14.

(21) Xu, C.; Nasrollahzadeh, M.; Selva, M.; Issaabadi, Z.; Luque, R. Waste-to-Wealth: Biowaste Valorization into Valuable Bio(Nano)-Materials. *Chem. Soc. Rev.* **2019**, *48* (18), 4791−4822.

(22) Wang, F.; Wu, X.; Yuan, X.; Liu, Z.; Zhang, Y.; Fu, L.; Zhu, Y.; Zhou, Q.; Wu, Y.; Huang, W. Latest Advances in Supercapacitors: From New Electrode Materials to Novel Device Designs. *Chem. Soc. Rev.* **2017**, *46* (22), 6816−6854.

(23) Hu, C.; Li, M.; Qiu, J.; Sun, Y. P. Design and Fabrication of Carbon Dots for Energy Conversion and Storage. *Chem. Soc. Rev.* **2019**, *48* (8), 2315−2337.

(24) Maruthasalamoorthy, S.; Aishwarya, K.; Thenmozhi, R.; Nirmala, R.; Nagarajan, C.; Navamathavan, R. Superior Cyclic Stability and Electrochemical Performance of La Supported Bi_2S_3@ g-C_3N_4//RGO Heterostructure Composite for Asymmetric Supercapacitor Devices. *J. Alloys Compd.* **2023**, *967*, No. 171696.

(25) Subramanian, M.; Violet Dhayabaran, V.; Shanmugavadivel, M. Fiber Optic Gas Sensing Properties of $Ni_2V_2O_7$ Nanorods Operable at Room Temperature. *Mater. Sci. Eng., B* **2020**, *259*, No. 114604.

(26) Liu, C.; Li, C.; Ahmed, K.; Mutlu, Z.; Ozkan, C. S.; Ozkan, M. Template Free and Binderless NiO Nanowire Foam for Li-Ion Battery Anodes with Long Cycle Life and Ultrahigh Rate Capability. *Sci. Rep.* **2016**, *6*, 1−8.

(27) Khan, A. Z.; Khan, I.; Sufyan, A.; Anjum, D.; Qurashi, A. Activation of $Ni_2V_2O_7$ to Nonstoichiometric NiV_3O_8 for Solar-Driven Photoelectrochemical Water Oxidation. *J. Environ. Chem. Eng.* **2021**, *9* (4), No. 105526.

(28) Ni, S.; Wang, X.; Zhou, G.; Yang, F.; Wang, J.; He, D. Crystallized $Zn_3(VO_4)_2$: Synthesis, Characterization and Optical Property. *J. Alloys Compd.* **2010**, *491* (1−2), 378−381.

(29) Mondal, C.; Ganguly, M.; Sinha, A. K.; Pal, J.; Sahoo, R.; Pal, T. Robust Cubooctahedron $Zn_3V_2O_8$ in Gram Quantity: A Material for Photocatalytic Dye Degradation in Water. *CrystEngComm* **2013**, *15* (34), 6745−6751.

(30) Bhujel, R.; Rai, S.; Baruah, K.; Deka, U.; Biswas, J.; Swain, B. P. Capacitive and Sensing Responses of Biomass Derived Silver Decorated Graphene. *Sci. Rep.* **2019**, *9* (1), 1−14.

(31) Elessawy, N. A.; El Nady, J.; Wazeer, W.; Kashyout, A. B. Development of High-Performance Supercapacitor Based on a Novel Controllable Green Synthesis for 3D Nitrogen Doped Graphene. *Sci. Rep.* **2019**, *9* (1), 1−10.

(32) Wei, C.; Huang, Y.; Xue, S.; Zhang, X.; Chen, X.; Yan, J.; Yao, W. One-Step Hydrothermal Synthesis of Flaky Attached Hollow-Sphere Structure $NiCo_2S_4$ for Electrochemical Capacitor Application. *Chem. Eng. J.* **2017**, *317*, 873−881.

(33) Venkatesan, D.; Annamalai, T.; Ramkumar, S.; Kanagajothi, D.; Karthik, P. S. Carbon - Supported Co_9S_8 Hollow Spheres Assembled from Ultrathin Nanosheets for High - Performance Supercapacitors. *J. Mater. Sci. Mater. Electron.* **2024**, *35* (16), 1−13.
(34) Sun, X.; Wang, L.; Li, C.; Wang, D.; Sikandar, I.; Man, R.; Tian, F.; Qian, Y.; Xu, L. Dandelion-Like Bi_2S_3/RGO Hierarchical Microspheres as High- Performance Anodes for Potassium-Ion and Half/Full Sodium-Ion Batteries. *Nano Res.* **2021**, *12* (1), 4696.
(35) Ghosh, K.; Srivastava, S. K. Superior Supercapacitor Performance of Bi2S3nanorod/Reduced Graphene Oxide Composites. *Dalt. Trans.* **2020**, *49* (46), 16993−17004.
(36) Manikandan, R.; Savariraj, A. D.; Nagaraju, G.; Kale, A. M.; Puigdollers, J.; Park, H.; Kim, H. S.; Oh, J. M.; Raj, C. J.; Kim, B. C. Mixed-Phase Composites Derived from Cobalt Terephthalate as Efficient Battery-Type Electrodes for High-Performance Supercapattery. *J. Mater. Sci. Technol.* **2023**, *157*, 220−233.
(37) Huang, Y.; Feng, X.; Li, C.; Li, Y.; Chen, X.; Gao, X.; Chen, C.; Guang, Z.; Liu, P. Construction of Hydrangea-like $ZnCo_2O_4/Ni_3V_2O_8$ Hierarchical Nanostructures for Asymmetric All-Solid-State Supercapacitors. *Ceram. Int.* **2019**, *45* (12), 15451−15457.
(38) Palani, S.; Veerasamy, U. S.; Mona, Y.; Chaichana, C.; Suttakul, P.; Wanison, R. Results in Engineering Facile Synthesis of RGO Nanosheet Encapsulated $Ni_2V_2O_7$ Nanorods for Energy Storage Applications. *Results Eng.* **2024**, *22*, No. 102134.
(39) Zhang, P.; Zhang, W.; Wang, Z.; Wang, X.; Ren, Q.; Zhang, S.; Wang, Y.; He, L.; Liu, P.; Zhang, Q.; Shi, Z. High-Voltage, Low-Temperature Supercapacitors Enabled by Localized "Water-in-Pyrrolidinium Chloride. *Electrolyte. eScience* **2023**, *3* (6), No. 100184.
(40) Yin, L.; Ouyang, Z.; Yue, X.; Wang, Z.; Xia, Z. High Magnetic Field ESR in S = 1 Skew Chain Antiferromagnet $Ni_2V_2O_7$ Single Crystal. *Crystals* **2019**, *9* (9), 468−9.

https://doi.org/10.1021/acsomega.4c08731
ACS Omega 2024, 9, 51481−51493